Check for updates

Advanced Synthesis & Catalysis

ADVANCED SYNTHESIS & CATALYSIS
advsynthcatal.com

RESEARCH ARTICLE OPEN ACCESS

Cu-ERI Zeolite Catalysts With Tailored Properties for the Removal of N-Containing Compounds

Magdalena Jabłońska[1,2] | Ana Palčić[3] | Yu Luo[4] | Pranjit Das[5] | Marko Bertmer[5] | Marek Rotko[6] | Andreas Pöppl[5] | Junjiang Zhu[4]

[1]Institute of Chemical Technology, Universität Leipzig, Leipzig, Germany | [2]Faculty of Chemistry, Department of Inorganic and Analytical Chemistry, University of Łódź, Łódź, Poland | [3]Laboratory for Synthesis of New Materials, Division of Materials Chemistry, Ruđer Bošković Institute, Zagreb, Croatia | [4]Hubei Key Laboratory for Clean Recycling and Resource Utilization of Waste Fibers, School of Chemistry and Environmental Engineering, Wuhan Textile University, Wuhan, China | [5]Felix Bloch Institute for Solid State Physics, Universität Leipzig, Leipzig, Germany | [6]Department of Chemical Technology, Institute of Chemical Sciences, Faculty of Chemistry, Maria Curie-Sklodowska University, Lublin, Poland

Correspondence: Magdalena Jabłońska (magdalena.jablonska@chemia.uni.lodz.pl)

Received: 15 May 2026 | **Revised:** 16 September 2026 | **Accepted:** 30 September 2026

Keywords: copper species | erionite | modulated excitation operando infrared spectroscopy | NH_3-SCO | NH_3-SCR-DeNO$_x$

ABSTRACT

A series of ERI-type zeolite materials of different properties was prepared, which led to the obtaining of Cu-containing ERI materials of distinct catalytic properties in the selective catalytic reduction of NO_x with ammonia (NH_3-SCR-DeNO$_x$) and the selective catalytic oxidation of ammonia (NH_3-SCO). Various characterization techniques were employed to describe the copper species in the synthesized ERI zeolite in order to understand its NH_3-SCR-DeNO$_x$ and NH_3-SCO activity as well as N_2 selectivity. Cu-ERI_1 and Cu-ERI_2 possess the highest amount of active sites (i.e., Cu^{2+} species) and thus enhanced activity in the low-temperature range of NH_3-SCR-DeNO$_x$ (with NO conversion of 83%–93% and N_2 selectivity of 93%–95% at 250 °C). Especially, Cu-ERI_2 possesses easily reducible Cu^{2+} species that are responsible for activation and oxidation of NH_3. Indeed, steady-state isotopic transient kinetic analysis of NH_3-SCO revealed the shortest average surface lifetime and the lowest surface concentration of NH_3 over the Cu-ERI_2 sample. Further, modulation excitation experiments confirmed that NO preferentially consumes NH_3 adsorbed on the Brønsted acid sites on this sample. For other samples, the experiments of NO absorption followed by $NH_3 + O_2$ exposure and around (NH_3 adsorption and $NO + O_2$ exposure) indicated that NH_3 adsorbed on Lewis acid sites is preferentially consumed during the reaction process.

1 | Introduction

The selective catalytic reduction with ammonia (NH_3-SCR-DeNO$_x$) stands out as the most efficient technology for eliminating NO_x from diesel engine exhausts, achieving removal efficiencies up to 95% [1]. Since the 1980s, metal-exchanged zeolites—including Fe-Beta and Cu-ZSM-5—have been the focus of extensive research for NH_3-SCR-DeNO$_x$ owing to their wide operating temperature range and excellent N_2 selectivity [2, 3]. Catalysts, which commonly encompass metal-exchanged zeolites, are an integral part of the NH_3-SCR-DeNO$_x$ in automobile applications [4, 5]. The selective catalytic oxidation of ammonia (NH_3-SCO) into nitrogen and water vapor is commonly performed after the NH_3-SCR-DeNO$_x$ unit to avoid NH_3 slip of exhaust gases from the after treatment system [6, 7]. Since the commercial application of Cu-SSZ-13 in 2010 in diesel engines, there has been a focus of research on small-pore size zeolites due to their high hydrothermal stability and long-lasting performance in NH_3-SCR-DeNO$_x$. A range of small-pore zeolites has been examined for this purpose, notably LTA, AFX, AEI, KFI, RHO, and ERI (e.g., [8, 9]). However, these materials can be obtained in a limited chemical composition, morphology, and particle size distribution, properties that directly

This is an open access article under the terms of the Creative Commons Attribution License, which permits use, distribution and reproduction in any medium, provided the original work is properly cited.

© 2026 The Author(s). *Advanced Synthesis & Catalysis* published by Wiley-VCH GmbH.

affect their performance in a given application. This work represents a contribution to these efforts by investigating the catalytic action of a series of ERI-type materials in NH_3-SCR-DeNO$_x$.

Erionite (ERI) is a small-pore zeolite framework built from erionite (*eri*) cages, cancrinite (*can*) cages, and double six-ring (*d6r*) units. The *can* cages and *eri* cavities are interconnected through shared four- and six-membered rings, as well as double six-membered rings [10]. Linking the *eri* cavities via common eight-membered rings results in the formation of a three-dimensional channel system. The ERI topology is part of the ABC-6 family, defined by an AABAAC stacking sequence. However, natural ERI zeolite has limited practical applicability owing to its low n(Si)/n(Al) ratio (ca. 3) and complex composition [11, 12]. UOP researchers first synthesized high-silica ERI zeolite using the charge density mismatch (CDM) approach, naming the material UZM-12 [13]. This approach generally uses a large amount of organic structure-directing agents (OSDAs) to create a CDM barrier that is later removed to induce crystallization, leading to long synthesis times (several days) for UZM-12. Relative to natural ERI zeolite, UZM-12 has a higher n(Si)/n(Al) ratio (>5.5). The synthesis of high-silica ERI zeolite has also been achieved by employing a bulky OSDA together with modified FAU zeolite as the source of silica and aluminum [14]. Recently, it was reported that ERI zeolite synthesized rapidly (2 h at 210 °C) shows markedly improved hydrothermal stability compared with conventional ERI zeolite, which is attributed to a reduced number of silanol defects [15, 16]. In addition, high silica ERI-type material was prepared from rationally designed OSDA, yet solely in the presence of potassium [16]. Overall, the synthesis procedure of zeolite ERI is delicate and sophisticated, and thus, only one commercially available product exists currently on the market [17]. The other reason for this could be that there are not many commercial processes that can apply zeolite ERI.

The ERI structure, with its unique structural and compositional features, creates particular microenvironments for Cu^{2+} species. The ERI framework features a small-pore, cage-type topology, with cationic positions predominantly at Site I (cage center), Site II (near the eight-membered ring windows), and Sites III and III' (within the six-membered rings) [18]. Cage-type zeolite materials, such as SSZ-13 (CHA-type), SSZ-16 (AFX-type), and SSZ-17 (LEV-type), exhibit highly similar structures and, consequently, similar exchangeable sites. It should be emphasized that the cationic positions outlined above denote the potential sites for Cu ions in dehydrated catalysts. However, during catalytic conditions of NH_3-SCR-DeNO$_x$ or NH_3-SCO, Cu ions are sufficiently solvated and will not occupy these sites. NH_3-SCR-DeNO$_x$ over Cu-containing zeolite-based catalysts was confirmed to follow a reduction half-cycle (RHC; $Cu^{2+} \rightarrow Cu^{+}$) and an oxidation half-cycle (OHC; $Cu^{+} \rightarrow Cu^{2+}$) (e.g., [19, 20]). The NH_3-SCR-DeNO$_x$ and NH_3-SCO catalytic activities are governed by the combined contributions of reducible Cu species and surface Brønsted acid sites (BAS), with their relative importance depending on the reaction temperature. In the low-temperature range, the catalytic activity is strongly associated with the amount of easily reducible Cu species, which can participate in the redox processes involved in the reactions. As the temperature increases, the contribution of surface BAS becomes more pronounced, particularly through their role in NH_3 adsorption and activation [21, 22]. Despite advances, elucidating and regulating the interplay between NH_3 adsorption and surface redox cycles continues to be a central challenge in optimizing NH_3-SCR-DeNO$_x$ and NH_3-SCO activity and N_2 selectivity. Developing small-pore zeolites with controlled compositions is key to designing advanced N-containing removal catalysts.

Taking these challenges into account in this work, we report the synthesis of high-silica ERI zeolite according to four different procedures. The prepared ERI-type zeolite materials were ion exchanged with copper species and investigated for their activity and N_2 selectivity in NH_3-SCR-DeNO$_x$ and NH_3-SCO. Using temperature-programmed studies (also with isotopically labeled NH_3), steady-state isotopic transient kinetic analysis (SSITKA), and operando diffuse reflectance infrared Fourier transform spectroscopy (DRIFTS), we linked the properties of the host structure with the material's acid and redox properties. Such insights shed light on the cooperative function of acid–redox networks and establish foundational principles for the rational development of active and N_2-selective NH_3-SCR-DeNO$_x$ and NH_3-SCO catalysts.

2 | Experimental Section

2.1 | Catalyst Preparation

Erionite-type zeolite sample (ERI) has been prepared according to the procedure adopted from [15, 23] using 0.28 g of aluminum-tri-sec-butoxide (Thermo Fischer, 97 wt.%) and 12.43 g of tetraethylammonium hydroxide (TEAOH, Alfa Aesar, 35 wt.%), stirred at room temperature and followed by dropwise addition of 5.46 g Ludox AS-40 (Sigma-Aldrich). Further, 1.65 g of hexamethonium bromide ((Hex)Br_2, TCI, 98 wt.%) was added to this mixture at once while stirring. A solution of 0.25 g of potassium chloride (KCl, Kemika, p.a.) and 5.02 g of doubly distilled water produced in our laboratory was prepared. This solution was added dropwise to the stirred synthesis mixture to obtain a molar oxide composition: 1 SiO_2:0.015 Al_2O_3:0.092 KCl:0.81 TEAOH:0.13 (Hex)Br_2:25 H_2O. Upon 24 h aging at room temperature under stirring, the synthesis mixture was transferred to an orbital shaker preheated at 75 °C and shaken at 250 rpm for 30 days. The sample prepared according to this procedure was named ERI_1.

The other sample—ERI_2—was prepared by the procedure adopted from [24]. Sodium aluminate ($NaAlO_2$, Riedel de Haën, $w(Al_2O_3) = 54$ wt.%, $w(Na_2O) = 41$ wt.%), KOH (Gram-mol, 89 wt.%), and NaOH (Gram-mol, 99 wt.%) were dissolved in doubly distilled water. Then, choline chloride (ChCl, Acros, 99 wt.%) and Ludox HS-30 (Aldrich) were admixed to form a reaction mixture of the following molar oxide composition: 1 SiO_2:0.05 Al_2O_3:0.7 NaOH:0.11 KOH:0.4 ChCl:15.6 H_2O. The mixture was subjected to hydrothermal treatment at 100 °C for 30 days.

ERI_3 was also prepared by the procedure adopted from [24]. A solution of $Al_2(SO_4)_2 \times 18$ H_2O (Kemika, p.a.) in doubly distilled water was mixed with a solution of water glass (Fluka, $w(SiO_2) = 27$ wt.%, $w(Na_2O) = 41$ wt.%) in doubly distilled water. Then, KOH (Gram-mol, 89 wt.%) and choline chloride were admixed (ChCl, Acros, 99 wt.%), yielding a reaction mixture of the following molar oxide composition: 1 SiO_2:0.04 Al_2O_3:0.8

16154169, 2026, 21, Downloaded from https://advanced.onlinelibrary.wiley.com/doi/10.1002/adsc.70834 by Ruder Boskovic Institute, Wiley Online Library on [19/11/2025]. See the Terms and Conditions (https://onlinelibrary.wiley.com/terms-and-conditions) on Wiley Online Library for rules of use; OA articles are governed by the applicable Creative Commons License

TABLE 1 | Synthesis parameters of the samples.

Sample	Reaction mixture composition	Time, d	*t*, °C
ERI_1	1 SiO_2:0.015 Al_2O_3:0.092 KCl:0.81 TEAOH:0.13 (Hex)Br_2:25 H_2O	30	75
ERI_2	1 SiO_2:0.05 Al_2O_3:0.7 NaOH:0.11 KOH:0.4 ChCl:15.6 H_2O	30	100
ERI_3	1 SiO_2:0.04 Al_2O_3:0.8 NaOH:0.8 KOH:0.4 ChCl:21.3 H_2O	120	100
ERI_4	1 SiO_2:0.04 Al_2O_3:2 NaOH:0.8 KOH:0.4 ChCl:15.6 H_2O	8	150

NaOH:0.8 KOH:0.4 ChCl:21.3 H_2O. This mixture was subjected to hydrothermal treatment at 100 °C for 120 days.

Finally, the sample, named ERI_4, was also prepared by the procedure adopted from [24]. Sodium aluminate ($NaAlO_2$, Riedel de Haën, $w(Al_2O_3) = 54$ wt.%, $w(Na_2O) = 41$ wt.%), KOH (Gram-mol, 89 wt.%), and NaOH (Gram-mol, 99 wt.%) were dissolved in doubly distilled water. Then, choline chloride (ChCl, Acros, 99 wt.%) and Ludox HS-30 (Aldrich) were added to give a synthesis mixture having molar oxide composition: 1 SiO_2:0.04 Al_2O_3:2 NaOH:0.8 KOH:0.4 ChCl:15.6 H_2O. This mixture was subjected to hydrothermal treatment at 150 °C for 8 days. Table 1 summarizes reaction mixture composition and reaction conditions for the samples prepared in these studies.

The final products were recovered by filtration and washed repeatedly until the pH value of the supernatant reached 7. The obtained solid was calcined at 550 °C for 4 h and was subsequently subjected to three consecutive ion exchanges with 0.5 M aqueous solution of ammonium nitrate at 80 °C for 1 h. The protonic zeolite forms were obtained by calcining the ammonium-exchanged CHA-type materials at 550 °C for 4 h in static air. Further, the samples were ion exchanged with 0.05 M aqueous solution of copper(II) acetate at room temperature for 24 h. Finally, the materials were calcined at 550 °C for 4 h.

2.2 | Catalyst Characterization and Catalytic Experiments

The basic physicochemical characterization techniques of the Cu-containing ERI samples were applied, including X-ray diffraction (XRD), N_2 sorption, nuclear magnetic resonance (NMR), electron paramagnetic resonance (EPR), scanning electron microscopy (SEM), inductively coupled plasma–optical emission spectroscopy (ICP–OES), as well as temperature-programmed methods (i.e., NH_3-TPD and H_2-TPR). Catalytic experiments cover NH_3-SCR-DeNO_x, NH_3-SCO, stop flow, and SSITKA

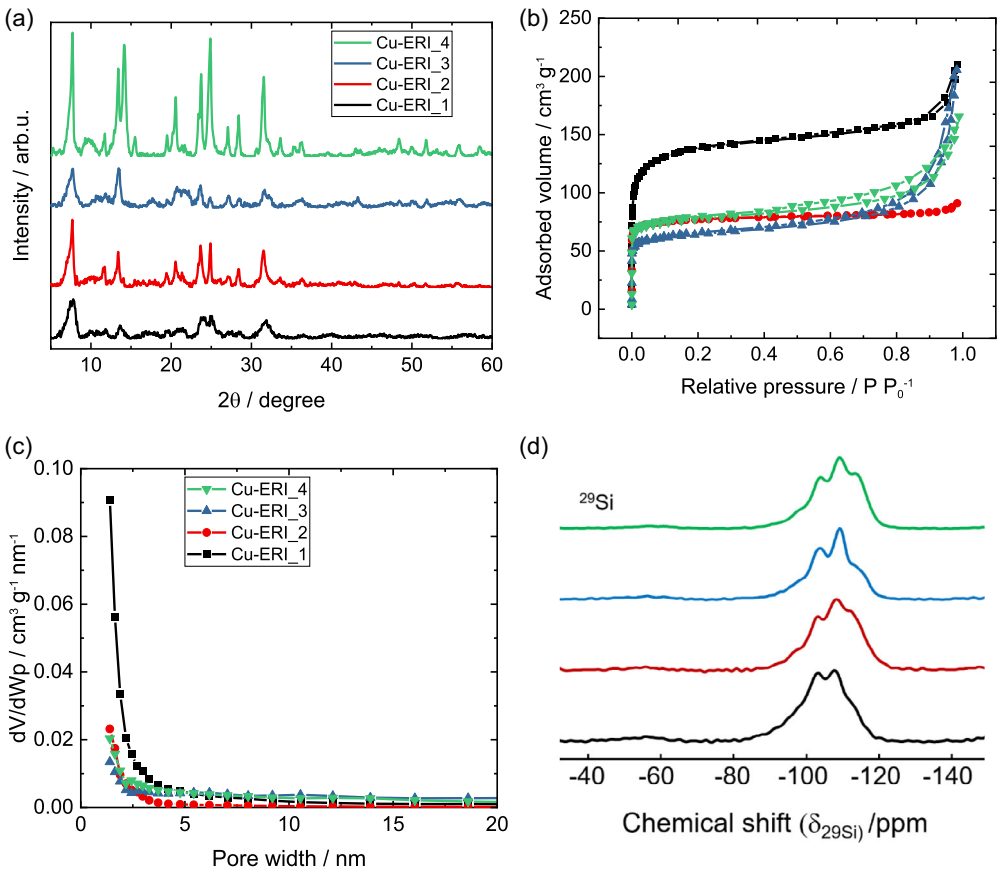

FIGURE 1 | (a) XRD patterns, (b) N_2 sorption isotherms, (c) pore width distribution, as well as (d) ^{29}Si MAS spectra of the Cu-containing ERI zeolite samples. Sample labels in (a–d) are the same.

16154169, 2026, 21, Downloaded from https://advanced.onlinelibrary.wiley.com/doi/10.1002/adsc.70834 by Ruder Boskovic Institute, Wiley Online Library on [19/11/2025]. See the Terms and Conditions (https://onlinelibrary.wiley.com/terms-and-conditions) on Wiley Online Library for rules of use; OA articles are governed by the applicable Creative Commons License

investigations, as well as operando DRIFTS and MS coupled study of surface adsorbates. Details concerning the applied techniques and experiments can be found in the Supporting Information.

3 | Results and Discussion

3.1 | Structural and Textural Properties

Figure 1a presents the XRD patterns of ERI zeolites, demonstrating that all samples are crystalline ERI-type materials [11]. N_2 sorption analysis further confirmed the high crystallinity of the Cu-containing zeolite ERI. Cu-ERI_3 possessed a significant contribution of mesopores with pore width of up to 5 nm (Figure 1c). The specific surface area of the samples varied in the range from 240 to 520 $m^2 g^{-1}$ (Table S1). ^{27}Al MAS NMR spectra in Figure S1 show one main peak at ca. 55–57 ppm for all Cu-ERI samples, indicating that Al species were incorporated in the ERI zeolite framework with tetrahedral coordination. Otherwise, for Cu-ERI_1 and Cu-ERI_4, we detected a small contribution of five- and sixfold coordinated Al species, respectively. Figures 1d and S2 show the contribution of different Si coordination to the area of the ^{29}Si NMR spectra of the Cu-containing ERI zeolite samples, with deconvolution shown in Table S2. Depending on how many aluminum tetrahedra share oxygen atoms with the SiO_4 unit, five distinct species can be identified: $Si(OSi)_4$, $Si(OAl)(OSi)_3$, $Si(OAl)_2(OSi)_2$, $Si(OAl)_3(OSi)$, and $Si(OAl)_4$ [25, 26]. However, recently, Zhu et al. [27] reported that the ERI zeolite contains two topologically distinct tetrahedral (T) sites, with multiplicities of 24 and 12, respectively, giving a total of 36 T atoms per unit cell (where T represents either Si or Al).

The T1 sites are located in hexagonal prisms, while the T2 sites are situated in the single six-membered rings of the *eri* cage, leading to different chemical shifts for a given species in the two sites (see assignment in Table S2). In the obtained Cu-containing ERI zeolites, the distinct tetrahedral sites' contribution varied significantly without any clear correlation. Among the samples, Cu-ERI_1 contains the highest amount of sites with higher Al coordination. Cu-ERI_2 and Cu-ERI_4 otherwise represent more Si sites with 0 or 1 Al coordination. In our earlier studies, the significant contribution of Si(3Si,1Al) was also detected in the most active and N_2-selective Cu-Y catalysts [28, 29]. This would correspond to samples Cu-ERI_3 and Cu-ERI_4 in the present study.

Table 2 shows the results of elemental analysis of the Cu-containing ERI zeolite samples. The highest copper loading

TABLE 2 | Results of the elemental analysis of the Cu-containing ERI zeolite samples (ω_i: mass fractions).

Sample	ω_{Si}, wt.%	ω_{Al}, wt.%	ω_{Cu}, wt.%	n(Si)/n(Al)	n(Cu)/n(Al)
Cu-ERI_1	30.3	5.3	5.3	5.5	0.42
Cu-ERI_2	31.9	4.3	4.1	7.1	0.41
Cu-ERI_3	33.3	3.9	2.8	8.2	0.31
Cu-ERI_4	33.2	5.5	2.9	5.8	0.22

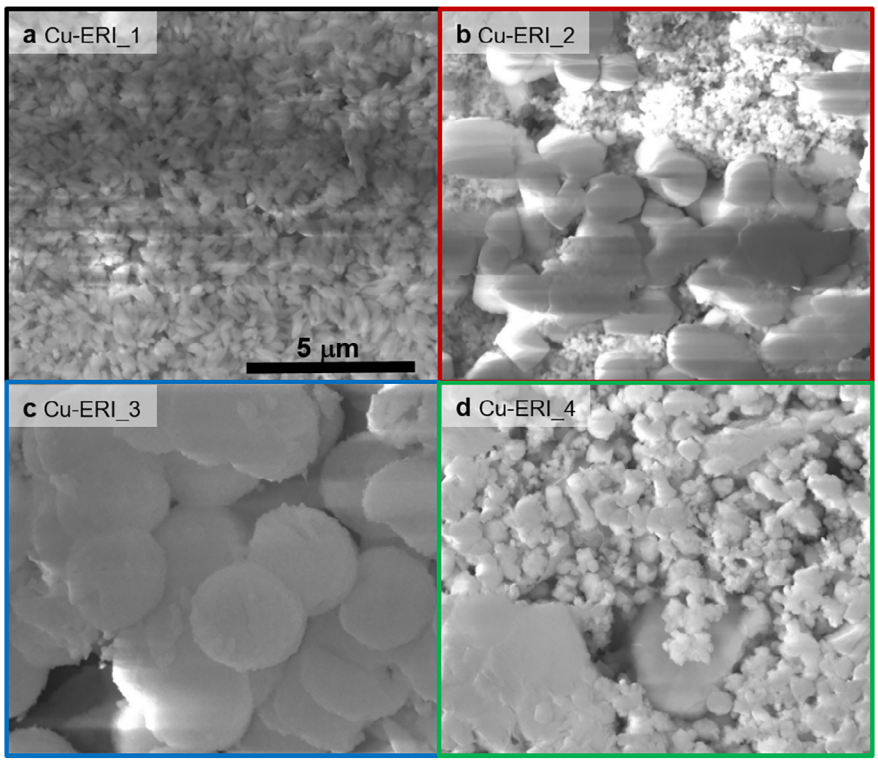

FIGURE 2 | (a–d) SEM images of the Cu-containing ERI zeolite samples. (a–d) The scale bar is the same.

16154169, 2026, 21, Downloaded from https://advanced.onlinelibrary.wiley.com/doi/10.1002/adsc.70834 by Ruder Boskovic Institute, Wiley Online Library on [19/11/2026]. See the Terms and Conditions (https://onlinelibrary.wiley.com/terms-and-conditions) on Wiley Online Library for rules of use; OA articles are governed by the applicable Creative Commons License

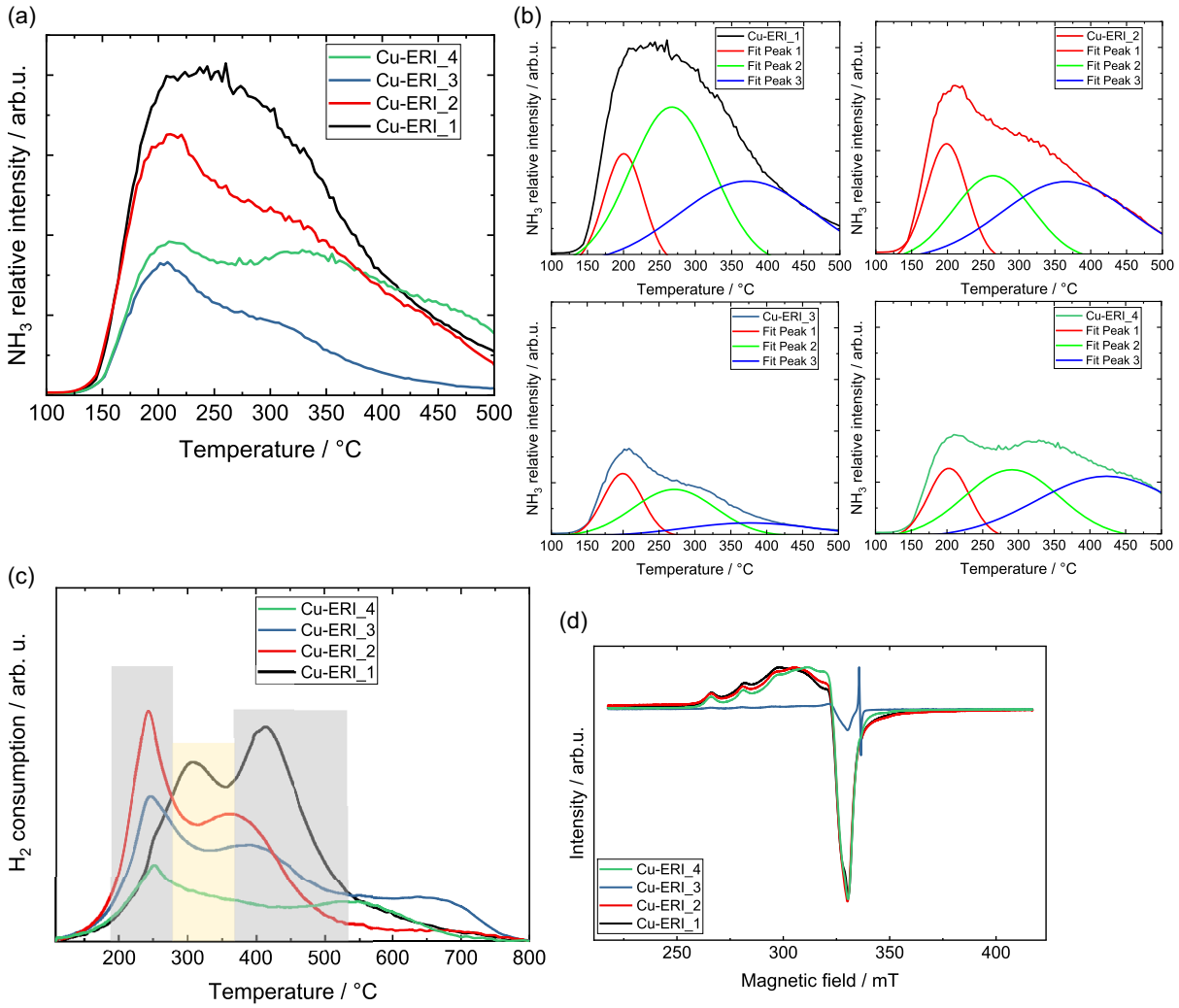

FIGURE 3 | (a) NH_3-TPD profiles and (b) the deconvolution of such profiles, as well as (c) H_2-TPR profiles of the Cu-containing ERI zeolite samples and (d) EPR profiles of activated Cu-containing ERI zeolite samples.

was detected for Cu-ERI_1 and Cu-ERI_2, while for the two other samples, the Cu loading was below 3 wt.%. The n(Cu)/n(Al) ratio below 0.5 indicates that all ion-exchanged positions are fully occupied without Cu species on the external surface of zeolites. Specifically, it should be noted that aluminum in the zeolite framework carries a negative charge and therefore requires charge-compensating cations [20, 30]. This is especially interesting for Cu-ERI_2, which shows the highest contribution of $Si(OSi)_4$ species. Copper content varied among samples depending on the applied initial zeolite ERI sample. In our studies, we applied the same ion exchange procedure as before for commercial zeolites [31, 32]. Still, some comparison is possible, especially for the materials with nearly the same n(Cu)/n(Al) ratio of 0.41–0.42, i.e., Cu-ERI_1 and Cu-ERI_2.

The SEM images in Figure 2 depict that the ERI zeolites exhibited distinct morphologies, including elongated elipsoids sphere-like shapes (for Cu-ERI_1) and spheres composed of intergrown particles (Cu-ERI_3) and cubic-like and sphere-like shapes (Cu-ERI_2, Cu-ERI_3, and Cu-ERI_4). The samples Cu-ERI_2 and Cu-ERI_4 constitute two different populations of particles, different in size, yet with rounded edges. The size of the particles of the investigated samples varied significantly. Recently, we have found that the size of SSZ-13 samples correlated with the copper content in Cu-SSZ-13 after the ion exchange procedure [19]. Although ERI is also in the group of small-pore zeolites, there is no clear correlation between copper content and particle sizes for Cu-containing ERI samples. These data support that all zeolite topologies should be investigated separately as there is no data model transferable for each zeolite.

3.2 | Acid–Redox Properties

Figure 3a,b shows temperature-programmed methods, i.e., desorption with ammonia (NH_3-TPD) and reduction with hydrogen (H_2-TPR). The desorption of ammonia for all materials starts around 150 °C and ends at 500 °C. Due to technical reasons, the measurement above 500 °C was not possible. The intensity of the desorption peak increased with copper species loading, with the effect more pronounced for Cu-ERI_2 and Cu-ERI_1 samples. For all materials (besides Cu-ERI_1), three desorption peaks are visible, i.e., below 250 °C, between 250–350 °C, and below 500 °C. To facilitate peak assignment, the NH_3-TPD profiles were deconvoluted by fitting three Gaussian curves, as shown in Figure 3b.

16154169, 2026, 21, Downloaded from https://advanced.onlinelibrary.wiley.com/doi/10.1002/adsc.70834 by Ruder Boskovic Institute, Wiley Online Library on [19/11/2026]. See the Terms and Conditions (https://onlinelibrary.wiley.com/terms-and-conditions) on Wiley Online Library for rules of use; OA articles are governed by the applicable Creative Commons License

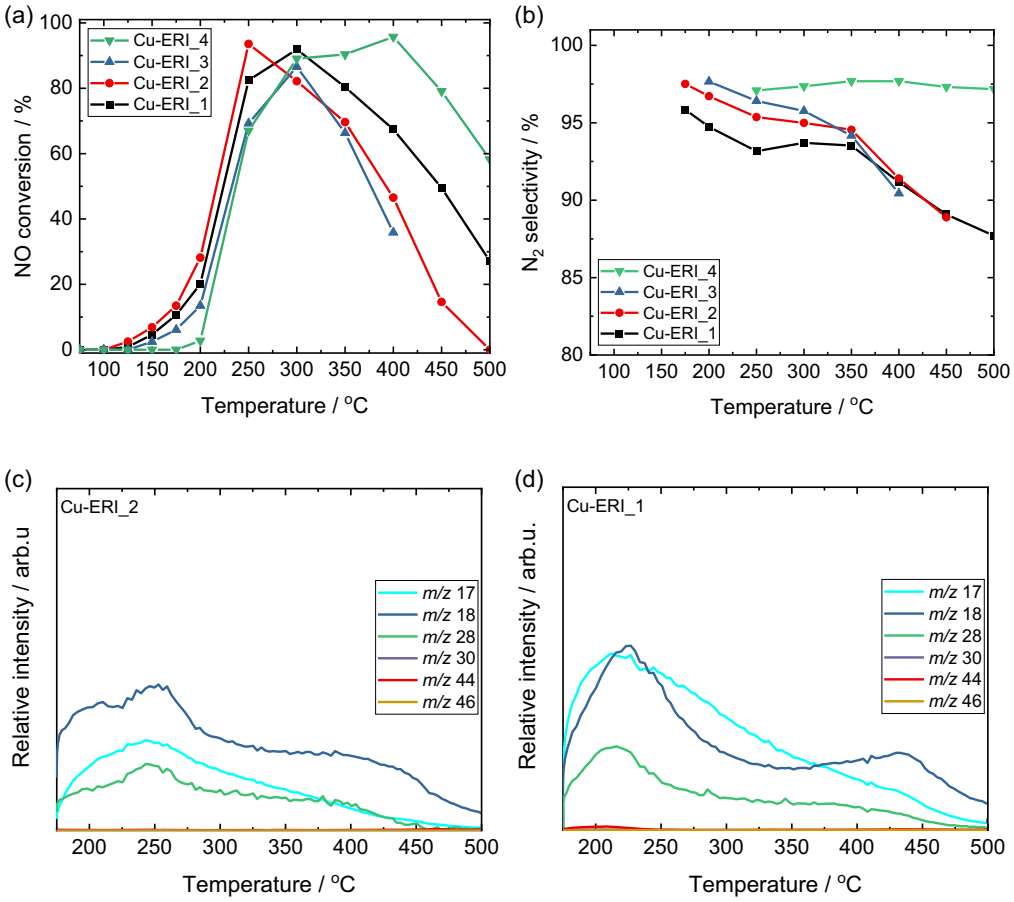

FIGURE 4 | (a) NO conversion and (b) N_2 selectivity during NH_3-SCR-DeNO$_x$ over Cu-containing ERI samples; (a) and (b) the sample names are the same. (c, d) Stop-flow experiments over (c) Cu-ERI_2 and (d) Cu-ERI_1 samples. Reaction conditions: $m_K = 0.1$ g, $c(NO) = 0.1$ vol.%, $c(NH_3) = 0.1$ vol.%, $c(O_2) = 5$ vol.%, He balance, $F_{TOT} = 120$ ml min^{-1}, GHSV = 30 000 h^{-1}.

The assignments of the peaks are challenging (e.g., [33, 34]). In our previous studies [32], we found two main peaks in NH_3-TPD for commercial ERI modified with copper species (n(Si)/n(Al) = 3.4, 6.1 wt.% of Cu). The NH_3 desorption peak at around 300 °C was assigned to NH_3 adsorbed on the Lewis acid sites (LAS), while the desorption peak centered at 440 °C was assigned to NH_3 adsorbed as NH_4^+ on BAS. In the present series of samples, the NH_3-TPD profile of Cu-containing zeolite ERI samples can be roughly deconvoluted into three pronounced peaks. The first desorption peaks below 250 °C are attributed to weakly bound NH_3 species [18]. According to Borfecchia et al. [35], $NH_4^+ \cdot n NH_3$ ($n \geq 1$) complexes form during NH_3 adsorption, and their subsequent decomposition contributes to the low-temperature desorption peak. The high-temperature desorption peak can be attributed to NH_3 desorption from BAS [36, 37]. The intermediate peak can be assigned to NH_3 adsorbed over Cu^{2+} sites [34, 38]. Among all samples, Cu-ERI_2 revealed a significant amount of adsorbed NH_3 compared to NH_3 adsorbed on Cu^{2+} sites.

Figure 3c shows the H_2-TPR profile of Cu-containing ERI samples. Similar to NH_3-TPD, three peaks can be distinguished in the H_2-TPR profile related to the low-temperature reduction peak of Cu^{2+} to Cu^+, medium-temperature reduction peak of Cu_xO_y species to Cu^0, and high-temperature reduction peak of Cu^+ to Cu^0 (e.g., [39, 40]). Also, in this case, the assignment of the peak can change and depends mostly on the copper loading. For Cu-ERI_2, we observed a narrow low-temperature peak between 200 and 300 °C, indicating the enhanced redox properties of the copper species present in the sample. Furthermore, the second reduction peak indicates the reduction of both Cu_xO_y species and Cu^+ to the metallic copper form. Both samples Cu-ERI_3 and Cu-ERI_4 present three reduction peaks; however, in this case, the lower copper content species and their higher interaction with the zeolite host led to lower reducibility of the present Cu species. Zhu et al. [16] reported that at low ion exchange levels (n(Cu)/n(Al) = 0.11), Cu^{2+} species preferentially occupy strongly interacting lattice sites and are therefore less reducible. At higher exchange levels, extra Cu^{2+} cations reside at weaker interaction sites and become more easily reducible. However, the Cu-ERI_1 sample possesses different reduction behavior. For this sample, only a small contribution of low-temperature species was present. The majority of the Cu^{2+} is reduced below 350 °C. Above 350 °C, a significant contribution of Cu^+ is reduced.

The EPR spectra of the as-synthesized samples are shown in Figure S3 and indicate that two species are needed for simulating the EPR spectra. An anisotropic species A with $g_{xx,yy} = 2.07$ (1), $g_{zz} = 2.39$ (2), and $A_{xx,yy} = 20$ (5) MHz and $A_{zz} = 400$ (5) MHz and a species B with an isotropic signal at $g = 2.17$ (2) have been used in the spectral simulations. Depending on the room-temperature EPR parameters, species A can be assigned to a copper hexa-aqua

16154169, 2026, 21, Downloaded from https://advanced.onlinelibrary.wiley.com/doi/10.1002/adsc.70834 by Ruder Boskovic Institute, Wiley Online Library on [19/11/2026]. See the Terms and Conditions (https://onlinelibrary.wiley.com/terms-and-conditions) on Wiley Online Library for rules of use; OA articles are governed by the applicable Creative Commons License

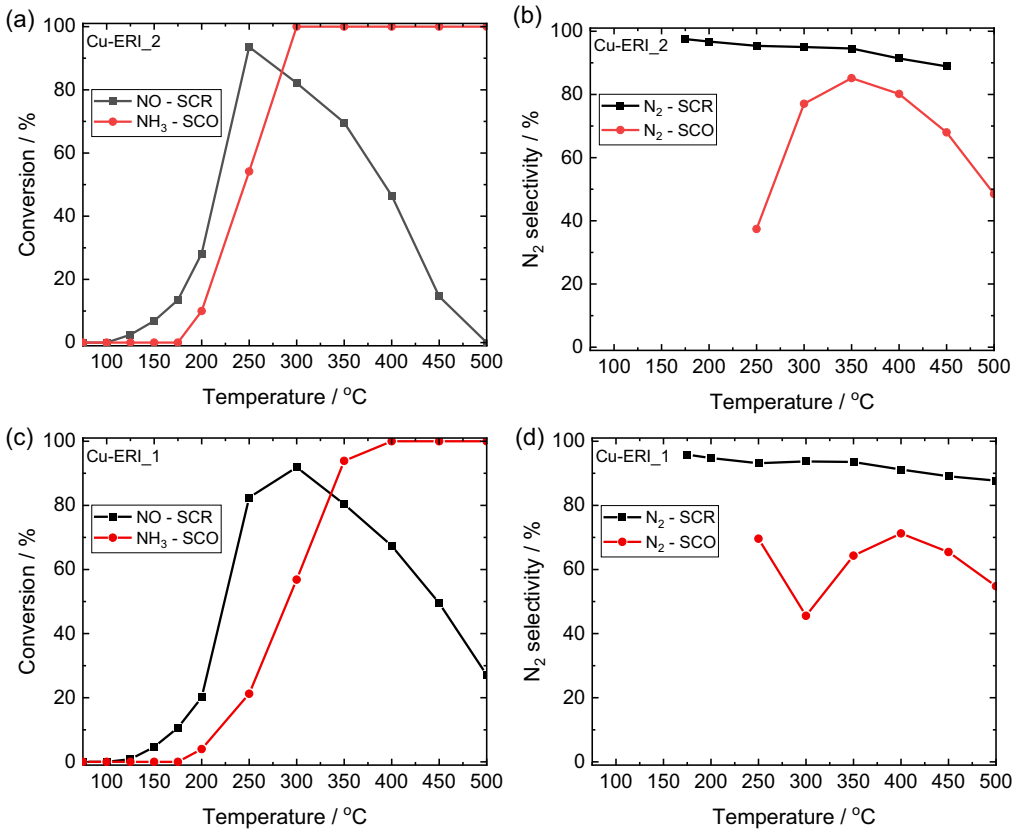

FIGURE 5 | Comparison of (a,b) the NO conversion during NH_3-SCR-DeNO$_x$ and NH_3 conversion during NH_3-SCO, as well as (c,d) comparison of N_2 selectivity in these two processes.

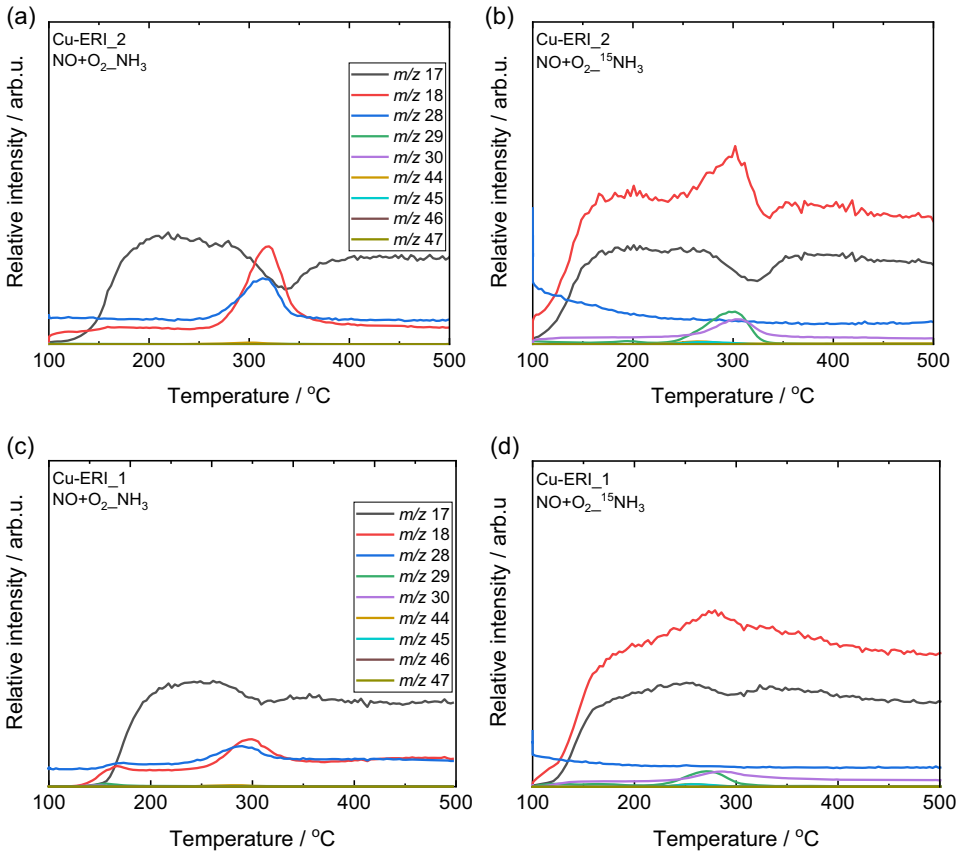

FIGURE 6 | Temperature-programmed desorption of NO + O_2 in NH_3 over (a) Cu-ERI_2, and (c) Cu-ERI_1, as well as of NO + O_2 in $^{15}NH_3$ over (b) Cu-ERI_2, and (d) Cu-ERI_1.

16154169, 2026, 21, Downloaded from https://advanced.onlinelibrary.wiley.com/doi/10.1002/adsc.70834 by Ruder Boskovic Institute, Wiley Online Library on [19/11/2025]. See the Terms and Conditions (https://onlinelibrary.wiley.com/terms-and-conditions) on Wiley Online Library for rules of use; OA articles are governed by the applicable Creative Commons License

water complex present in the sample [41, 42]. Anticorrelated g and A strains are used to simulate the broadening effect of the EPR lines with increasing m_I (spin quantum numbers) value. For this case, $g_{strain} = 0.008$ and $A_{strain} = 10$ MHz are used. The line shape for species A is a Voigtian line shape with Gaussian broadening of 3 mT and Lorentzian broadening of 2 mT; and for species B, a Lorentzian line shape with broadening of 10 mT is used. As the g value of B corresponds to the isotropic g value of species A, we assign species B to a motional averaged spectrum of species A and consequently to $[Cu(H_2O)_6]^{2+}$ complexes that undergo fast tumbling. The weights of species A and B used for simulation of the EPR spectra are shown in Table S3.

Then, the samples were activated under a vacuum of 1 mbar and heated up to 200 °C overnight (Figure S4). Such an activation procedure changes the EPR parameters of the samples. Two different species are found with an anisotropic species C, $g_{xx,yy} = 2.07$ (1), $g_{zz} = 2.34$ (2), and $A_{xx,yy} = 50$ (5) MHz and $A_{zz} = 450$ (5) MHz and a species D providing an isotropic signal at $g = 2.16$ (1). It has been reported earlier that species A from the as-synthesized sample loses some of its water ligand and migrates to different sites in the zeolite upon activation, which can be observed as species C [41, 42]. Again, an anticorrelated g and A strain is used to simulate the line broadening with increasing m_s value. For this case, $g_{strain} = 0.02$ and $A_{strain} = 10$ MHz are used. The line shape used for species C is a Voigtian line shape with Gaussian broadening of 1 mT and Lorentzian broadening of 2 mT. For species D, a Lorentzian line with broadening of 10 mT is implemented. As the g value of species D corresponds to the isotropic g value of species C, we assign D to Cu^{2+} species C in high local concentrations. In such a case, magnetic dipole and exchange interactions among the cupric ions lead to an isotropic EPR signal with a

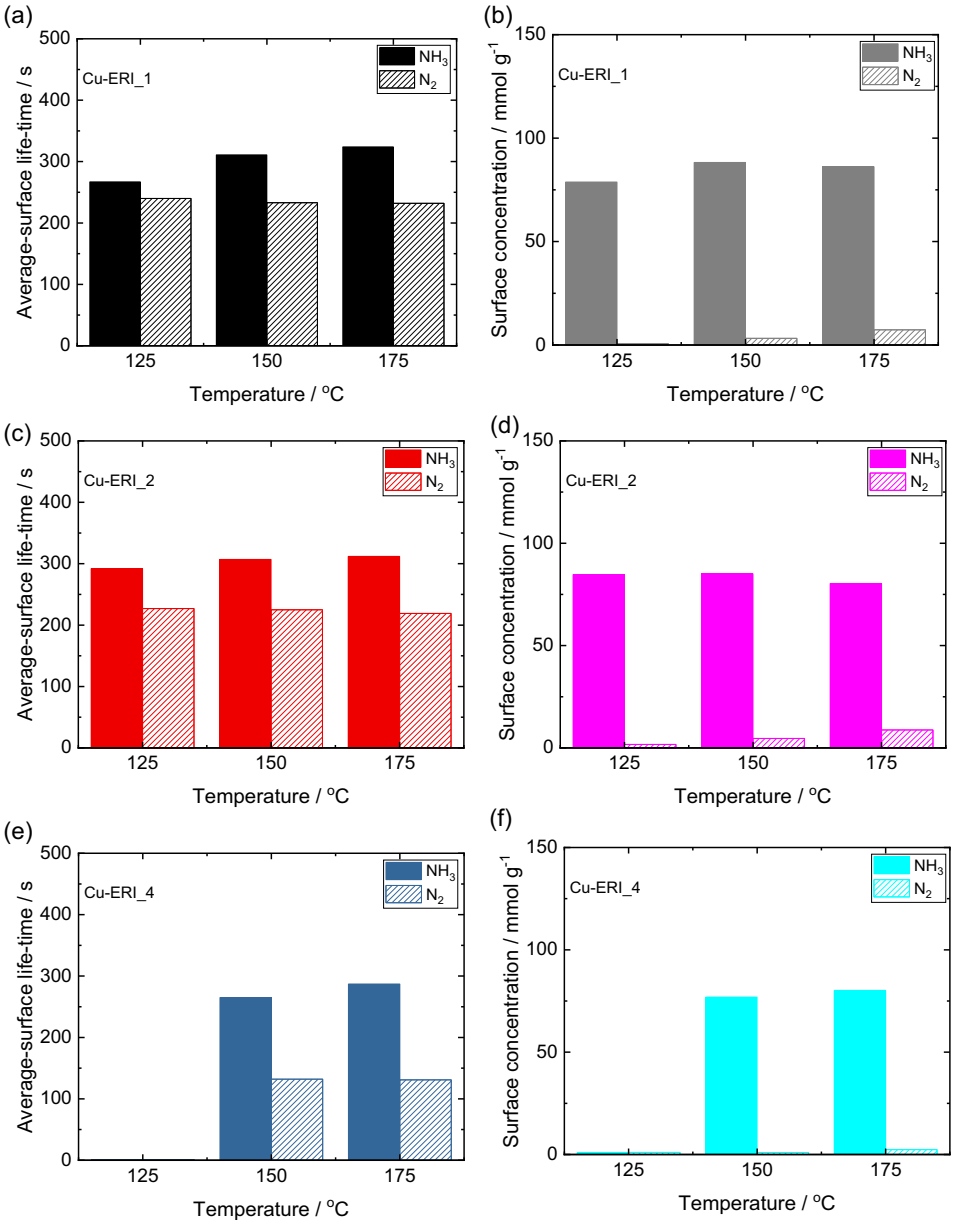

FIGURE 7 | (a,c,e) Average surface lifetime of reversibly adsorbed ammonia, adsorbed nitrogen molecules, and intermediates leading to the formation of nitrogen during NH_3-SCR-DeNO$_x$, and (b,d,f) surface concentration of reversibly adsorbed ammonia, adsorbed nitrogen molecules, and intermediates leading to the formation of nitrogen.

16154169, 2026, 21, Downloaded from https://advanced.onlinelibrary.wiley.com/doi/10.1002/adsc.70834 by Ruder Boskovic Institute, Wiley Online Library on [19/11/2026]. See the Terms and Conditions (https://onlinelibrary.wiley.com/terms-and-conditions) on Wiley Online Library for rules of use; OA articles are governed by the applicable Creative Commons License

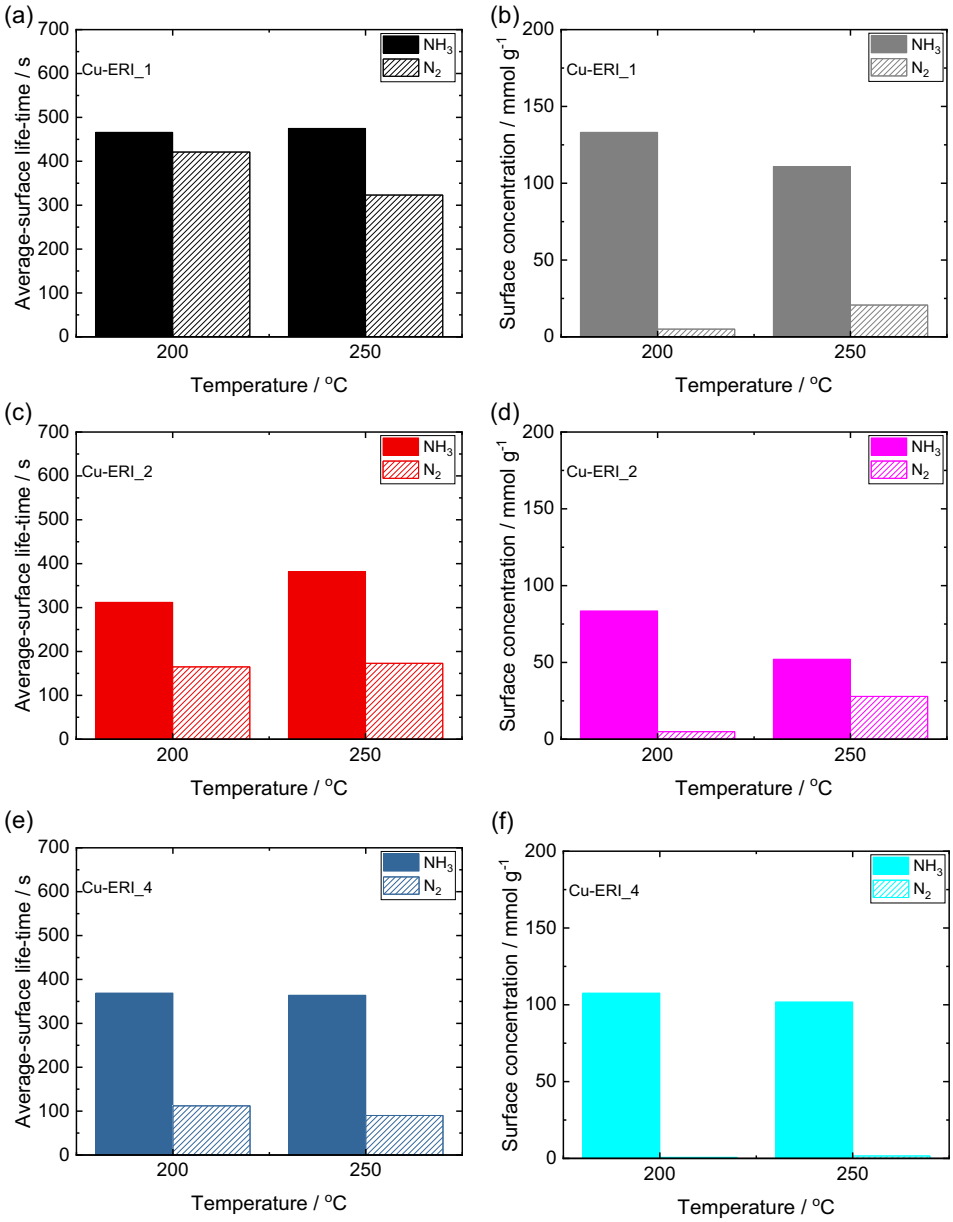

FIGURE 8 | (a,c,e) Average surface lifetime of reversibly adsorbed ammonia, adsorbed nitrogen molecules, and intermediates leading to the formation of nitrogen during NH_3-SCO, and (b,d,f) surface concentration of reversibly adsorbed ammonia, adsorbed nitrogen molecules, and intermediates leading to the formation of nitrogen.

g value corresponding to the isotropic *g* value of isolated species (here *C*). A tumbling motion for species *A*, as often observed for $[Cu(H_2O)_6]^{2+}$ complexes in hydrated and as-synthesized samples, can be ruled out here for the activated case, as for the dehydrated samples, the copper hexa-aqua water complex does not exist anymore. The weights of species *C* and *D* for the simulation of the EPR spectra are shown in Table S4. Thus, the catalyst activity in the NH_3-SCR-DeNO$_x$ follows the amount of Cu^{2+} species (i.e., species *D*).

3.3 | Insight Into NH_3-SCR-DeNO$_x$ and NH_3-SCO

The Cu-containing ERI zeolite samples were investigated in the NH_3-SCR-DeNO$_x$ and NH_3-SCO. Different copper species content and their characteristic have driven the reaction differently. As shown in Figures 4a and S5, the highest activity in NH_3-SCR-DeNO$_x$, i.e., below 200 °C, was found for Cu-ERI_2, followed by Cu-ERI_1 and Cu-ERI_3 catalysts. However, in these cases, a rather narrow activity window was found. Zhu et al. [27] focused on the zeolite ERI with different *n*(Si)/*n*(Al) ratios. They reported that the catalyst with a *n*(Cu)/*n*(Al) ratio of 0.20 showed a high activity comparable to the commercial NH_3-SCR-DeNO$_x$ catalyst between 200 and 600 °C. This composition was assigned to accommodate the maximum amount of isolated Cu^{2+} species [16]. This is also valid in our case for this temperature range as the Cu-ERI_4 catalysts possess the highest activity and N_2 selectivity (Figure 4a,b). Although other samples show lower N_2 selectivity, this is still above 90% below 400 °C (the rest constitute N_2O, Figure S5). A comparison of the investigated Cu-ERI_2 with other Cu-containing samples prepared from commercially available SSZ-13, ZSM-5, and ERI zeolites revealed

16154169, 2026, 21, Downloaded from https://advanced.onlinelibrary.wiley.com/doi/10.1002/adsc.70834 by Ruder Boskovic Institute, Wiley Online Library on [19/11/2026]. See the Terms and Conditions (https://onlinelibrary.wiley.com/terms-and-conditions) on Wiley Online Library for rules of use; OA articles are governed by the applicable Creative Commons License

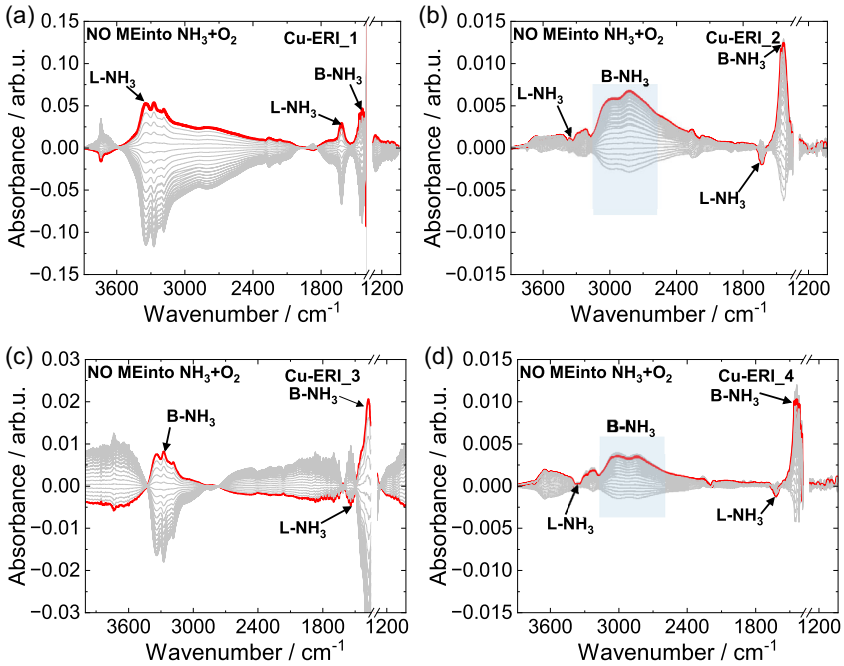

FIGURE 9 | Phase domain in situ IR spectra of NO adsorption and $NH_3 + O_2$ exposure on (a) Cu-ERI_1, (b) Cu-ERI_2, (c) Cu-ERI_3, and (d) Cu-ERI_4.

significantly lower NO_x conversion for Cu-ERI_2 (Figure S6). However, the reaction conditions used for these samples were different, which should be taken into account when comparing their catalytic performance.

Further investigation into the NH_3-SCR-DeNO$_x$ process was carried out via stop-flow experiments (Figures 4c,d and S7). In this case, the NH_3-SCR-DeNO$_x$ was carried out for 2 h at 125 °C and then 3 h of He purging and a temperature rise in the presence of He flow. Based on these studies, we could identify adsorbed species that do not take part in the reaction. The significant contribution—especially for Cu-ERI_2 and Cu-ERI_1—is attributed to NH_3. Water vapor and N_2 evolution probably arise due to NH_3 oxidation. For the other two catalysts (Figure S7), the contribution of the adsorbed NH_3 was significantly lower than for Cu-ERI_2.

To further explore catalytic properties from NH_3 activation and oxidation, we conducted NH_3-SCO over Cu-ERI-based samples. Figures S8 and S9 show NH_3 conversion and selectivity during NH_3-SCO, while Figure 5 shows the comparison between NH_3-SCR-DeNO$_x$ and NH_3-SCO, including N_2 selectivity in these two processes for selected samples. As can be seen, the decrease in activity during NH_3-SCR-DeNO$_x$ is driven by the NH_3 oxidation process above 300 °C. Although the Cu-ERI_1 possesses a higher content of copper species, the NH_3 oxidation is significantly more robust over Cu-ERI_2 sample (Figures S8 and S9). N_2 selectivity varied among samples and reactions, regarding the level and shape of the curve. A significantly higher N_2 selectivity was found in the NH_3-SCR-DeNO$_x$ for all samples.

Otherwise, during NH_3-SCO, the profile changes depending on the samples. Figure S8b compares N_2 selectivity among the applied samples. For most of them, N_2 selectivity sharply decreased and then exhibited a volcano shape. Only for Cu-ERI_2, there is no decrease in the N_2 selectivity, so the shape of the curve is a volcano shape only. This effect can be correlated with the reaction mechanism of NH_3-SCO. In the first step, NH_3 is oxidized to NO, while in the second step, the unreacted (in the first step, NH_3) is reduced to NO_x via NH_3-SCR-DeNO$_x$ [43, 44]. Correlation of these two processes led to enhanced N_2 selectivity. The comparison of these two catalytic processes for all samples (Figures 5 and S8c,d) shows that for Cu-ERI_2, the conversion curves of NH_3 and NO are well correlated. For other catalysts, i.e., Cu-ERI_1 and Cu-ERI_3, the conversion curves are more distinct. This statement is supported by the outcome for sample Cu-ERI_4, where the conversion curves are even more separated, which is reflected by the N_2 selectivity profile.

To further explore the interaction of NH_3 with the catalysts, we applied temperature-programmed studies. As the NH_3-SCR-DeNO$_x$ reaction mechanism has been proposed over different zeolites to follow reduction and oxidation half-cycles (e.g., [19, 20]), the temperature-programmed studies with adsorption of reactant molecules can serve as such half-cycles.

In our studies, a mixture of diluted NO + O_2 was passed through the material for 2 h; then, the surface was cleared with He for 3 h and finally heated up in the presence of diluted NH_3 or labeled $^{15}NH_3$. Figures 6 and S10 present the outcome of these studies. The comparison of the experiments shows formation of *m/z* 29 presenting N_2, from the oxidation of labeled NH_3 around 300 °C. Further comparison shows a significantly higher contribution to N_2 and water vapor for Cu-ERI_2 sample, indicating enhanced activation and conversion of NH_3 over this sample. Thus, the copper species present in this sample significantly activate and oxidize NH_3 compared to other samples. The redox properties determine the catalytic activity in NH_3-SCO, with a drop in selectivity to N_2 at higher temperatures, according to our previous studies (e.g., [45, 46]).

16154169, 2026, 21, Downloaded from https://advanced.onlinelibrary.wiley.com/doi/10.1002/adsc.70834 by Ruder Boskovic Institute, Wiley Online Library on [19/11/2025]. See the Terms and Conditions (https://onlinelibrary.wiley.com/terms-and-conditions) on Wiley Online Library for rules of use; OA articles are governed by the applicable Creative Commons License

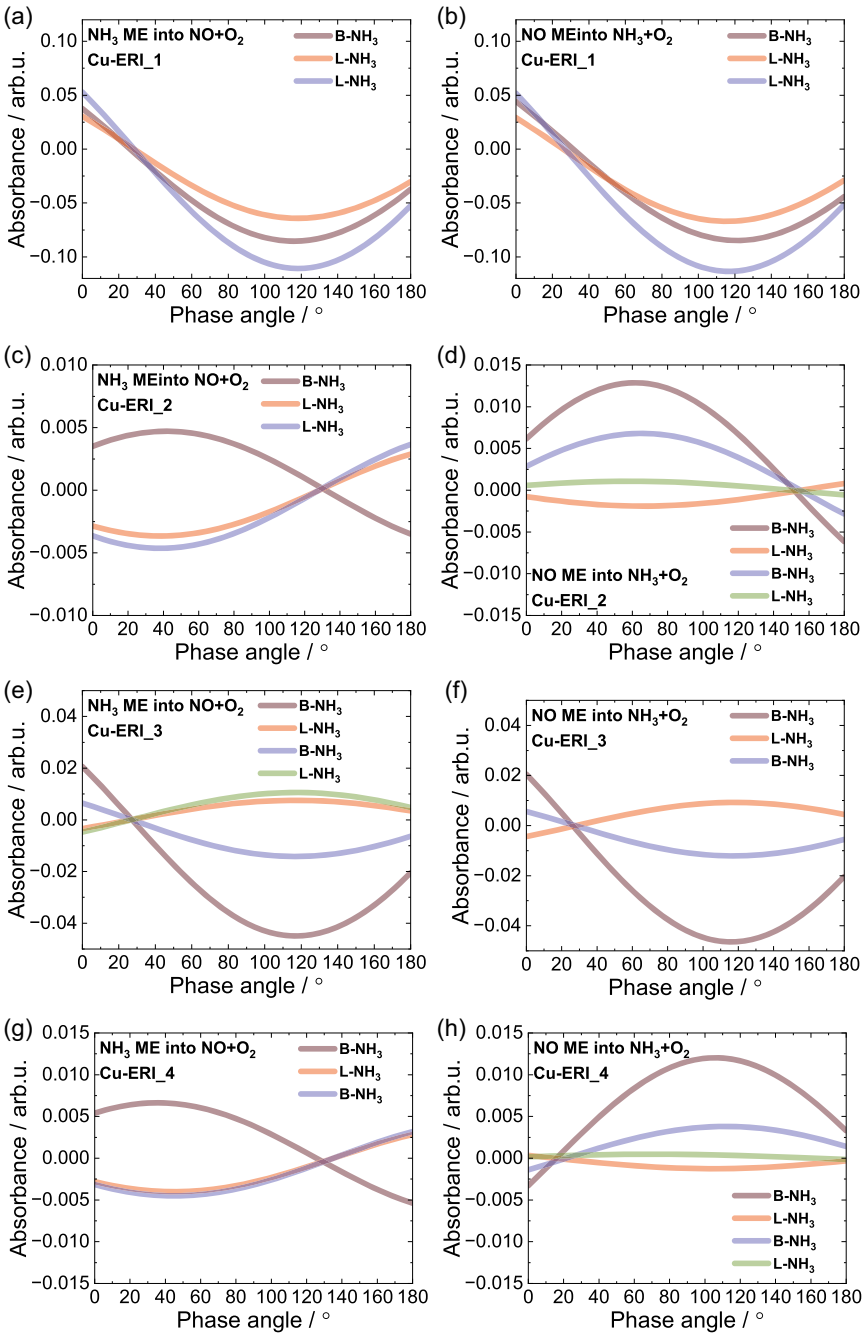

FIGURE 10 | Phase angle dependence of DRIFTS signal during NH_3 adsorption and NO + O_2 exposure on (a) Cu-ERI_1, (c) Cu-ERI_2, (e) Cu-ERI_3, and (g) Cu-ERI_4, and NO adsorption and $NH_3 + O_2$ exposure on (b) Cu-ERI_1, (d) Cu-ERI_2, (f) Cu-ERI_3, and (h) Cu-ERI_4.

Figures 7 and 8 show the steady-state isotopic kinetic transient (SSITKA) analysis with switching between NH_3 and $^{15}NH_3$. Measurements of the Cu-based ERI zeolite samples were performed at selected temperatures to keep the conversion below 20%. The Cu-ERI_4 sample was excluded from these measurements because it required a much higher temperature to achieve a significant conversion. Kinetic parameters such as the average surface lifetime and the surface concentration of NH_3, N_2, and intermediates leading to its formation were determined. During the NH_3-SCR-DeNO$_x$ process, the average surface lifetime of NH_3 increased with temperature for all catalysts, and also, practically the same situation is observed at higher temperatures during the NH_3-SCO process. For the surface concentration of NH_3, values during selective reduction are very similar across all catalysts and do not change significantly with temperature, whereas during NH_3 oxidation, a pronounced decrease is observed with rising temperature, especially on Cu-ERI_2 and Cu-ERI_1. It is correlated with TPD results (Figure 3a), which indicate intensive ammonia desorption above 200 °C. The average surface lifetime of N_2 and intermediates that lead to its formation during selective reduction slightly decreases with increasing temperature on the surface of all studied catalysts. Moreover, it is worth noting that the values of average surface lifetime are the lowest on the surface of Cu-ERI_3 because, in this case, the reciprocal of this kinetic parameter, interpreted as the average efficiency (intrinsic activity—TOF_{ITK}) of active centers [47, 48], is the highest. Although it offers the most

16154169, 2026, 21, Downloaded from https://advanced.onlinelibrary.wiley.com/doi/10.1002/adsc.70834 by Ruder Boskovic Institute, Wiley Online Library on [19/11/2026]. See the Terms and Conditions (https://onlinelibrary.wiley.com/terms-and-conditions) on Wiley Online Library for rules of use; OA articles are governed by the applicable Creative Commons License

effective active centers, this catalytic material is inferior to Cu-ERI_2 and Cu-ERI_1 (Figure 4a) because the number of such centers (surface concentration of N_2 and intermediates leading to its formation) is lower. In NH_3 oxidation, the average surface lifetime of N_2 and intermediates that lead to its formation clearly decreases with temperature for Cu-ERI_1 and Cu-ERI_3, while it remains unchanged for Cu-ERI_2. Moreover, the differences in values indicate the highest effectiveness of the active centers on the surface of Cu-ERI_3 and the lowest on Cu-ERI_1. On the other hand, the surface concentration of N_2 and intermediates that lead to its formation increases with temperature for all catalysts and is the highest on the surface of Cu-ERI_2. Lower values are observed for Cu-ERI_1 and the lowest for Cu-ERI_3. These results explain why the Cu-ERI_2 catalyst is the most active in the NH_3-SCO process (Figure S8).

Operando DRIFTS and modulation excitation (ME) experiments were also applied to investigate the reaction mechanism of NH_3-SCR-DeNO$_x$ and identify reactive surface species over Cu-containing (e.g., [19, 49]) and Ce-containing catalysts (e.g., [21, 50]). The application of ME IR technology and transient experiments to explore the involvement of LAS and BAS is of great significance. As shown by the phase-domain spectra obtained during NO modulation in $NH_3 + O_2$ (Figure 9), Cu-ERI_1 exhibits more pronounced changes in the DRIFTS signals of surface-adsorbed species than the other three samples, indicating a stronger spectroscopic response of these species to NO modulation. Notably, Cu-ERI_1 shows a positive correlation between NH_3 adsorbed on BAS (B-NH_3, 1439 cm^{-1}) and LAS (L-NH_3, 1619 cm^{-1}) upon NO modulation, indicating that both species respond concurrently to the periodic perturbation. In contrast, B-NH_3 and L-NH_3 exhibit a negative correlation for Cu-ERI_2, Cu-ERI_3, and Cu-ERI_4, where the increase in B-NH_3 is accompanied by the consumption of L-NH_3. Together with the phase domain analysis, these results suggest preferential involvement of L-NH_3 in the reaction with NO for these catalysts. The distinct behavior of Cu-ERI_1 points to a different balance between Brønsted- and Lewis-bound NH_3 species, likely associated with its different distribution of acid and Cu sites. Thus, the catalytic behavior is influenced not only by the amount of adsorbed NH_3 but also by its distribution and dynamic response on different acid sites.

From the test spectra of NH_3 ME in $NO + O_2$ (Figure S11), Cu-ERI_1 also exhibits a much stronger response than the other catalysts under pulsed NO conditions. Unlike the behavior observed during NO pulsing, a negative correlation between B-NH_3 and L-NH_3 is found for the Cu-ERI_2 sample, accompanied by an enhanced response of L-NH_3. This indicates that NO preferentially consumes B-NH_3, and the formation of both B-NH_3 and L-NH_3 is strongly correlated with NH_3.

The band near 3600 cm^{-1} assigned to surface —OH groups, as well as the absorption bands in the range from 1600 to 2600 cm^{-1} related to the catalyst framework structure, needs to be further analyzed in combination with the specific structural properties of the catalyst.

The B-NH_3 and L-NH_3 signals were individually extracted from the aforementioned in situ images to generate the corresponding phase distribution diagrams (Figure 10). The positive and negative correlations between various surface species, as well as their relative signal intensities, can be visualized more intuitively from these plots. This reveals that B-NH_3 exhibits a phase delay of 6° relative to L-NH_3, which indicates that L-NH_3 is preferentially consumed during the reaction process.

4 | Conclusions

The prepared ERI-type zeolite materials exhibited significantly different catalytic performances in NH_3-SCR-DeNO$_x$ and NH_3-SCO reactions as a consequence of variations in the nature and distribution of copper species. Among the investigated catalysts, Cu-ERI_1 and especially Cu-ERI_2 showed the highest concentration of catalytically active Cu^{2+} sites, resulting in superior low-temperature NH_3-SCR-DeNO$_x$ activity. The enhanced reducibility of Cu^{2+} species in Cu-ERI_2 additionally promoted efficient ammonia activation and oxidation, leading to improved NH_3-SCO performance. SSITKA measurements demonstrated that Cu-ERI_2 possessed the shortest ammonia surface lifetime and the lowest surface NH_3 concentration, confirming its high reactivity toward NH_3 oxidation. Moreover, ME studies revealed that for Cu-ERI_2, NH_3 adsorbed on BAS was preferentially involved in reaction with NO, whereas in the remaining catalysts, NH_3 coordinated to LAS played the dominant role in the reaction pathway. These findings provide important insight into the relationship between copper speciation, surface acidity, and catalytic behavior in ERI zeolites, contributing to the rational design of highly efficient DeNO$_x$ catalysts.

Author Contributions

Magdalena Jabłońska: methodology, conceptualization, investigation, data curation, writing – original draft, writing – review and editing, visualization, supervision. **Ana Palčić:** investigation, writing – review and editing. **Yu Luo:** investigation, data curation, writing – review and editing. **Pranjit Das:** investigation, data curation, writing – review and editing. **Marko Bertmer:** investigation, data curation. **Marek Rotko:** writing – review and editing. **Andreas Pöppl:** review. **Junjiang Zhu:** review.

Funding

This work was supported by the National Natural Science Foundation of China (No. 42277485) and the Department of Science and Technology of Hubei Province (No. 2024CSA084).

Open Access funding enabled and organized by Projekt DEAL.

Conflicts of Interest

The authors declare no conflicts of interest.

Data Availability Statement

The data that support the findings of this study are available from the corresponding author upon reasonable request.

References

1. M. Jabłońska, M. E. Potter, and A. M. Beale, "Recent Progress in the Application of Transition-Metal Containing MFI Topologies for NH_3-SCR-DeNO$_x$ and NH_3 Oxidation," *ChemCatChem* 16, (2023): e202301214, https://doi.org/10.1002/cctc.v16.5.

16154169, 2026, 21, Downloaded from https://advanced.onlinelibrary.wiley.com/doi/10.1002/adsc.70834 by Ruder Boskovic Institute, Wiley Online Library on [19/11/2026]. See the Terms and Conditions (https://onlinelibrary.wiley.com/terms-and-conditions) on Wiley Online Library for rules of use; OA articles are governed by the applicable Creative Commons License

2. M. Iwamoto, H. Furukawa, Y. Mine, F. Uemura, S.-I. Mikuriya, and S. Kagawa, "Copper(II) Ion-Exchanged ZSM-5 Zeolites as Highly Active Catalysts for Direct and Continuous Decomposition of Nitrogen Monoxide," *Journal of the Chemical Society, Chemical Communications*. (1986): 1272–1273, https://doi.org/10.1039/c39860001272.

3. O. Mihai, C. R. Widyastuti, S. Andonova, et al., "The Effect of Cu-Loading on Different Reactions Involved in NH_3-SCR Over Cu-BEA Catalysts," *Journal of Catalysis* 311 (2014): 170–181, https://doi.org/10.1016/j.jcat.2013.11.016.

4. M. Jabłońska, "Review of the Application of Cu-Containing SSZ-13 in NH_3-SCR-DeNO$_x$ and NH_3-SCO," *RSC Advances* 12 (2022): 25240–25261, https://doi.org/10.1039/D2RA04301G.

5. M. Jabłońska, "Recent Progress in the Selective Catalytic Reduction of NO_x With NH_3 on Cu-SAPO-34 Catalysts," *Molecular Catalysis* 518 (2022): 112111.

6. M. Jabłońska and R. Palkovits, "Copper Based Catalysts for the Selective Ammonia Oxidation Into Nitrogen and Water Vapour-Recent Trends and Open Challenges," *Applied Catalysis B: Environment and Energy* 181 (2016): 332–351.

7. L. Chmielarz and M. Jabłońska, "Advances in Selective Catalytic Oxidation of Ammonia to Dinitrogen: A Review," *RSC Advances* 5 (2015): 43408–43431.

8. J. Han, D. Li, and J. Yu, "Tailoring Cu-Based Small-Pore Zeolites Towards NH_3-SCR for NO_x Abatement," *Chemical Society Reviews* 54 (2025): 7933–7965.

9. G. Lee, D. J. Deka, K. G. Rappé, and J. Szanyi, "Water Effects on NH_3-SCR Over Cu-Based Small-Pore Zeolite Catalysts: A Review," *Applied Catalysis A: General*. (2025): 120491.

10. accessed Mai 2026, https://www.iza-structure.org/databases/.

11. J. H. Lee, M. B. Park, J. K. Lee, H.-K. Min, M. K. Song, and S. B. Hong, "Synthesis and Characterization of ERI-Type UZM-12 Zeolites and Their Methanol-to-Olefin Performance," *Journal of the American Chemical Society* 132 (2010): 12971–12982.

12. S. Seo, N. H. Ahn, J. H. Lee, et al., "Combined Alkali-Organoammonium Structure Direction of High-Charge-Density Heteroatom-Containing Aluminophosphate Molecular Sieves," *Angewandte Chemie* 131 (2019): 9130–9135.

13. M. A. Miller, G. J. Lewis, J. G. Moscoso, et al., "Synthesis and Catalytic Activity of UZM-12," in *Studies in Surface Science and Catalysis*. Elsevier (2007): 487–492.

14. N. Martín, C. Paris, P. N. R. Vennestrøm, J. R. Thøgersen, M. Moliner, and A. Corma, "Cage-Based Small-Pore Catalysts for NH_3-SCR Prepared by Combining Bulky Organic Structure Directing Agents With Modified Zeolites as Reagents," *Applied Catalysis B: Environment and Energy* 217 (2017): 125–136.

15. J. Zhu, Z. Liu, K. Iyoki, et al., "Ultrafast Synthesis of High-Silica Erionite Zeolites With Improved Hydrothermal Stability," *Chemical Communications* 53 (2017): 6796–6799.

16. J. Zhu, Z. Liu, L. Xu, et al., "Understanding the High Hydrothermal Stability and NH_3-SCR Activity of the Fast-Synthesized ERI Zeolite," *Journal of Catalysis* 391 (2020): 346–356.

17. accessed 14.05.2026, *Available at:* https://www.clariant.com/en/Business-Units/Catalysts/Zeolite-Powders/ERI.

18. H. Wang, R. Xu, Y. Jin, and R. Zhang, "Zeolite Structure Effects on Cu Active Center, SCR Performance and Stability of Cu-Zeolite Catalysts," *Catalysis Today* 327 (2019): 295–307.

19. A. M. Robles, M. Jabłońska, A. Palčić, et al., "Cu-SSZ-13 Catalysts Designed Through Interzeolite Conversion Process From Different Structure Types of Zeolites for NH_3-SCR-DeNO$_x$: Structure-Property Activity Relationships and Intermediates Determination," *ChemCatChem* 17, (2025): e01017.

20. K. A. Tarach, M. Jabłońska, K. Pyra, et al., "Effect of Zeolite Topology on NH_3-SCR Activity and Stability of Cu-Exchanged Zeolites," *Applied Catalysis B: Environment and Energy* 284 (2021): 119752.

21. J. Yang, Y. Luo, Z. Chen, and J. Zhu, "Synergistic Effects and Individual Roles of Ce-O–W Sites in the NH_3-SCR Redox Cycle-Acid Cycle," *Applied Catalysis B: Environment and Energy* (2026): 126430.

22. E. Groppo, S. Rojas-Buzo, and S. Bordiga, "The Role of *In Situ/Operando* IR Spectroscopy in Unraveling Adsorbate-Induced Structural Changes in Heterogeneous Catalysis," *Chemical Reviews* 123 (2023): 12135–12169, https://doi.org/10.1021/acs.chemrev.3c00372.

23. S. P. Sree, E. Verheyen, M. De Prins, et al., "Synthesis of a New Zeolite, Intergrowth of Erionite and Chabazite," *ACS Materials Letters* 3 (2021): 658–662.

24. US. patent 4116813

25. E. Lippmaa, M. Maegi, A. Samoson, M. Tarmak, and G. Engelhardt, "Investigation of the Structure of Zeolites by Solid-State High-Resolution Silicon-29 NMR Spectroscopy," *Journal of the American Chemical Society* 103 (1981): 4992–4996.

26. C. A. Fyfe, G. C. Gobbi, W. J. Murphy, R. S. Ozubko, and D. A. Slack, "Investigation of the Factors Affecting the 29Si MAS NMR Linewidths of Zeolites," *Chemistry Letters* 12 (1983): 1547–1550.

27. J. Zhu, K. Muraoka, T. Ohnishi, et al., "Synthesis and Structural Analysis of High-Silica ERI Zeolite With Spatially-Biased Al Distribution as a Promising NH_3-SCR Catalyst," *Advancement of Science* 11 (2024): 2307674.

28. M. Jabłońska, R. S. R. Suharbiansah, N. Zhang, et al., "Disclosing the Enhanced NH_3-SCR-DeNO$_x$ Activity of Cu-Containing Zeolite Y Prepared With 15-Crown-5," *Catalysis Today* 432 (2024): 114611.

29. M. Jabłońska, R. S. R. Suharbiansah, K. Góra-Marek, et al., "NH_3-SCR-DeNO$_x$ Activity of Cu-Containing Commercial Zeolite Y," *Industrial & Engineering Chemistry Research* 63 (2024): 17075–17085.

30. M. Jabłońska, K. Góra-Marek, P. C. Bruzzese, et al., "Influence of Framework *n*(Si)/*n*(Al) Ratio on the Nature of Cu Species in Cu-ZSM-5 for NH_3-SCR-DeNO$_x$," *ChemCatChem* 14, 2022): e202200627.

31. M. Jabłońska, A. M. Robles, M. Rotko, et al., "Unraveling the NH_3-SCR-DeNO$_x$ Mechanism of Cu-SSZ-13 Variants by Spectroscopic and Transient Techniques," *ChemSusChem* 17 (2024): e202400198.

32. A. M. Robles, G. Deplano, K. Góra-Marek, et al., "Post-Synthetically Treated ERI and SSZ-13 Zeolites Modified With Copper as Catalysts for NH_3-SCR-DeNO$_x$," *Catalysts* 14 (2024): 457, https://doi.org/10.3390/catal14070457.

33. B. Mozgawa, F. Zasada, M. Fedyna, et al., "Analysis of NH_3-TPD Profiles for CuSSZ-13 SCR Catalyst of Controlled Al Distribution-Complexity Resolved by First Principles Thermodynamics of NH_3 Desorption, IR and EPR Insight Into Cu Speciation," *Chemistry: A European Journal* 27 (2021): 17159–17180.

34. K. Leistner, K. Xie, A. Kumar, K. Kamasamudram, and L. Olsson, "Ammonia Desorption Peaks Can Be Assigned to Different Copper Sites in Cu/SSZ-13," *Catalysis Letters* 147 (2017): 1882–1890, https://doi.org/10.1007/s10562-017-2083-8.

35. E. Borfecchia, K. A. Lomachenko, F. Giordanino, et al., "Revisiting the Nature of Cu Sites in the Activated Cu-SSZ-13 Catalyst for SCR Reaction," *Chemical Science* 6 (2015): 548–563, https://doi.org/10.1039/C4SC02907K.

36. A. Izadbakhsh, F. Farhadi, F. Khorasheh, S. Sahebdelfar, M. Asadi, and Y. Z. Feng, "Effect of SAPO-34's Composition on Its Physico-Chemical Properties and Deactivation in MTO Process," *Applied Catalysis A: General* 364 (2009): 48–56, https://doi.org/10.1016/j.apcata.2009.05.022.

37. L. Rodríguez-González, F. Hermes, M. Bertmer, E. Rodríguez-Castellón, A. Jiménez-López, and U. Simon, "The Acid Properties of

16154169, 2026, 21, Downloaded from https://advanced.onlinelibrary.wiley.com/doi/10.1002/adsc.70834 by Ruder Boskovic Institute, Wiley Online Library on [19/11/2026]. See the Terms and Conditions (https://onlinelibrary.wiley.com/terms-and-conditions) on Wiley Online Library for rules of use; OA articles are governed by the applicable Creative Commons License

H-ZSM-5 as Studied by NH_3-TPD and ^{27}Al-MAS-NMR Spectroscopy," *Applied Catalysis A: General* 328 (2007): 174–182, https://doi.org/10.1016/j.apcata.2007.06.003.

38. I. Lezcano-Gonzalez, U. Deka, B. Arstad, et al., "Determining the Storage, Availability and Reactivity of NH_3 Within Cu-Chabazite-Based Ammonia Selective Catalytic Reduction Systems," *Physical Chemistry Chemical Physics* 16 (2014): 1639–1650, https://doi.org/10.1039/C3CP54132K.

39. M. Jabłońska, A. Palčić, M. F. Lukman, et al., "OSDA-Free Seeded Cu-Containing ZSM-5 Applied for NH_3-SCR-DeNO$_x$," *ACS Omega* 8 (2023): 41107–41119, https://doi.org/10.1021/acsomega.3c03721.

40. R. S. R. Suharbiansah, M. F. Lukman, C. Nannuzzi, et al., "Effect of the Preparation Method on the Catalytic Properties of Copper-Containing Zeolite Y Applied for NH 3-SCR-DeNO$_x$," *Catalysis Science & Technology* 13 (2023): 3804–3817, https://doi.org/10.1039/D3CY00269A.

41. A. Alberti, A. Martucci, E. Galli, and G. Vezzalini, "A Reexamination of the Crystal Structure of Erionite," *Zeolites* 19 (1997): 349–352, https://doi.org/10.1016/S0144-2449(97)00102-4.

42. J. S. Yu and L. Kevan, "Temperature Dependence of Copper (II) Migration and Formation of New Copper (II) Species During Catalytic Propylene Oxidation on Copper (II)-Exchanged Y Zeolite and Comparison With X Zeolite," *The Journal of Physical Chemistry* 94 (1990): 7612–7620, https://doi.org/10.1021/j100382a055.

43. L. Chmielarz, M. Jabłońska, A. Strumiński, et al., "Selective Catalytic Oxidation of Ammonia to Nitrogen Over Mg-Al, Cu-Mg-Al and Fe-Mg-Al Mixed Metal Oxides Doped With Noble Metals," *Applied Catalysis B: Environment and Energy* 130 (2013): 152–162.

44. M. Jabłońska, A. Król, E. Kukulska-Zajac, K. Tarach, L. Chmielarz, and K. Góra-Marek, "Zeolite Y Modified With Palladium as Effective Catalyst for Selective Catalytic Oxidation of Ammonia to Nitrogen," *Journal of Catalysis* 316 (2014): 36–46.

45. M. Jabłońska, K. Nothdurft, M. Nocuń, V. Girman, and R. Palkovits, "Redox-Performance Correlations in Ag-Cu-Mg-Al, Ce-Cu-Mg-Al, and Ga-Cu-Mg-Al Hydrotalcite Derived Mixed Metal Oxides," *Applied Catalysis B: Environment and Energy* 207 (2017): 385–396.

46. M. Jabłońska, "TPR Study and Catalytic Performance of Noble Metals Modified Al_2O_3, TiO_2 and ZrO_2 for Low-Temperature NH_3-SCO," *Catalysis Communications* 70 (2015): 66–71.

47. M. Jabłońska, "An Application of Steady-State Isotopic-Transient Kinetic Analysis (SSITKA) in DeNO$_x$ Process," *ChemCatChem* 13 (2021): 818–827.

48. C. Ledesma, J. Yang, D. Chen, and A. Holmen, "Recent Approaches in Mechanistic and Kinetic Studies of Catalytic Reactions Using SSITKA Technique," *ACS Catalysis* 4 (2014): 4527–4547, https://doi.org/10.1021/cs501264f.

49. M. Jabłońska, R. S. R. Suharbiansah, J. Yang, et al., "Modulated excitation DRIFTS and Steady-State Isotopic Transient Kinetic Analysis (SSITKA) of NH_3-SCR-DeNO$_x$ on Cu-Containing Zeolite Y," *Catalysis Science & Technology* 16 (2026): 1902–1912, https://doi.org/10.1039/D5CY01536G.

50. J. Yang, X. Li, S. Lyu, S. Wang, Z. Chen, and J. Zhu, "Brønsted-to-Lewis NH_3 Migration: An Elemental Step During Selective Catalytic Reduction of Nitric Oxide," *Applied Catalysis B: Environment and Energy* (2026): 126609, https://doi.org/10.1016/j.apcatb.2026.126609.

Supporting Information

Additional supporting information can be found online in the Supporting Information section.

16154169, 2026, 21, Downloaded from https://advanced.onlinelibrary.wiley.com/doi/10.1002/adsc.70834 by Ruder Boskovic Institute, Wiley Online Library on [19/11/2026]. See the Terms and Conditions (https://onlinelibrary.wiley.com/terms-and-conditions) on Wiley Online Library for rules of use; OA articles are governed by the applicable Creative Commons License